Dalton Transactions

PAPER

View Article Online
View Journal | View Issue

Cite this: *Dalton Trans.*, 2015, **44**, 18536

Structural phase transitions and photoluminescence properties of Eu^{3+} doped $Ca_{(2-x)}Ba_xLaNbO_6$ phosphors

Jicheng Zhu,[a] Zhiguo Xia,*[a] Yuanyuan Zhang,[b] Maxim S. Molokeev[c,d] and Quanlin Liu*[a]

Received 3rd September 2015,
Accepted 23rd September 2015

DOI: 10.1039/c5dt03430b

www.rsc.org/dalton

Crystal structures of the series of double perovskites $Ca_{(2-x)}Ba_xLaNbO_6:Eu^{3+}$ phosphors have been examined by powder X-ray diffraction and Rietveld refinements. Ca_2LaNbO_6 has a monoclinic ($P2_1/n$) and Ba_2LaNbO_6 has a monoclinic ($C2/m$) structure. The structural phases of $Ca_{(2-x)}Ba_xLaNbO_6:Eu^{3+}$ samples are divided into three sections depending on different Ca/Ba ratios: (1) monoclinic phase ($P2_1/n$) as Ca_2LaNbO_6 in the range of x = 0–0.1, (2) mixed phases containing Ca_2LaNbO_6 and Ba_2LaNbO_6 between 0.15 and 1.2, and (3) monoclinic phase ($C2/m$) as Ba_2LaNbO_6 for x = 1.4–2. Eu^{3+} ions act as the structural probes to study the structural phase transitions, and the evolution of the photoluminescence properties and thermal stability behaviours has been also comparatively investigated depending on different structural symmetries from Ca_2LaNbO_6 to Ba_2LaNbO_6 phase. The strong red emission from $^5D_0$–$^7F_2$ peaking at 618 nm can be found in $Ca_2LaNbO_6:Eu^{3+}$ phosphors, which is attributed to the low crystal field effect of the activator ions located in the highly distorted [LaO_8] polyhedra sites. The composition-optimized phosphors can find applications in white light emitting diodes (LEDs).

1. Introduction

ABO_3-type perovskite oxides, where A and B denote two different cations, are structurally stable because of their well-balanced geometrical array of constituent atoms and valances. Structural phase transitions in perovskites have long been of interest to solid-state chemists, and great efforts to determine the physical properties have also been extensively made, such as optical, ferroelectric, magnetic, and superconductor properties, by materials scientists. However, due to the relatively easy energy transfer when the B site is occupied by a transition metal, most of the perovskites are good magnetic materials but not excellent phosphor hosts.[1] However, ordered double perovskites with the general formula $A_2B'B''O_6$ are formed when the B site of ABO_3 is occupied by two different cations (B′ = rare earth elements, B″ = transition metal, d-block metals, such as Mo, Sb, Nb, Ta) in the disordered state; therefore double perovskite compounds may become suitable candidate phosphors by structurally modulating a series of elements in $A_2B'B''O_6$.[2–4] In addition, the $B'O_6$ and $B''O_6$ in $A_2B'B''O_6$ can reduce the symmetry of A sites and contribute a variety of environments for doping rare earth ions.[5]

The crystal structure of Ca_2LaNbO_6 has been first reported by Fillipev and Fesenko,[6] and Ba_2LaNbO_6 has also been studied in recent years.[7–10] Ca_2LaNbO_6 has a monoclinic ($P2_1/n$) and Ba_2LaNbO_6 has a monoclinic ($C2/m$) structure. There are two Ca sites in Ca_2LaNbO_6 and one site is occupied by the disordered 50% Ca and 50% La. However, there is only one Ba site and one La site in Ba_2LaNbO_6, and that's to say, La^{3+} ions in Ca_2LaNbO_6 and Ba_2LaNbO_6 have different coordination environments.

Owing to the great requirement for the red phosphors used in developing solid state lighting, such as white light emitting diodes (LEDs), many different types of hosts have been developed, such as $Ca_{14}Al_{10}Zn_6O_{35}:Mn^{4+}$,[11] $BaGeF_6:Mn^{4+}$,[12] $Li_6CaLa_2Sb_2O_{12}:Eu^{3+}$,[13] and so on. Among them, Eu^{3+}-doped red phosphors played an important role in these fields. In our present work, we have synthesized a series of double perovskite $Ca_{(2-x)}Ba_xLaNbO_6$ phosphors. By doping Eu^{3+} ions in La^{3+} sites, Eu^{3+} ions have changeable environments from Ca_2LaNbO_6 to Ba_2LaNbO_6, which is a complex process for the variation of the phase structures. Eu^{3+} ions can also act as

[a]*School of Materials Science and Engineering, University of Science and Technology Beijing, Beijing, 100083, China. E-mail: xiazg@ustb.edu.cn, qlliu@ustb.edu.cn; Fax: +86-10-82377955, +86-10-6233-4705; Tel: +86-10-82377955, +86-10-6233-4705*
[b]*School of Materials Sciences and Technology, China University of Geosciences, Beijing 100083, China*
[c]*Laboratory of Crystal Physics, Kirensky Institute of Physics, SB RAS, Krasnoyarsk 660036, Russia*
[d]*Department of Physics, Far Eastern State Transport University, Khabarovsk, 680021 Russia*

structural probes to study the structural phase transitions; moreover, the red emissions from the magnetic dipole transition ($^5D_0$–$^7F_1$) at about 596 nm and the electric dipole transition ($^5D_0$–$^7F_2$) at about 618 nm were observed when the samples were excited by near ultraviolet (396 nm) or blue light (465 nm) to match the commercial LED chips.

2. Experimental section

2.1 Materials and synthesis

A series of niobate-based double perovskite phosphors, $Ca_{(2-x)}Ba_xLa_{0.95}NbO_6$:0.05$Eu^{3+}$ ($0 \le x \le 2$), were synthesized by a traditional high temperature solid-state reaction. Since the main topic focused on is the effect of Ca/Ba ratios on the phase structural evolution and luminescence properties, the doping concentration of Eu^{3+} is fixed at 0.05 mol for all the studied samples. Stoichiometric amounts of $CaCO_3$ (A.R.), $BaCO_3$ (A.R.), La_2O_3 (99.99%), Nb_2O_5 (99.99%) and Eu_2O_3 (99.99%) were intimately mixed homogeneously in an agate mortar and then placed in alumina crucibles and fired at 1300 °C for 6 h. Finally, the samples were, after cooling to room temperature in the furnace, ground to fine powders for the following characterization.

2.2 Characterization

The phase structures of the $Ca_{(2-x)}Ba_xLaNbO_6$:Eu^{3+} samples were measured by using an X-ray diffractometer (D/max-rA 12 kW, Japan) with Cu-Kα radiation (λ = 0.15406 nm), operating at 40 kV, 35 mA. The continuous scanning rate (2θ ranging from 10° to 70°) was 4° (2θ) min^{-1} and the step scanning rate (2θ ranging from 10° to 100°) used for Rietveld analysis was 8 s per step with a step size of 0.02. Powder diffraction data were further analysed using a computer software TOPAS 4.2 program. Diffuse reflection spectra of the as-synthesized samples were recorded on a UV-Vis-NIR spectrophotometer (UV-3600, Shimadzu) attached to an integral sphere. $BaSO_4$ was used as a reference standard. The photoluminescence (PL) spectra and excitation (PLE) spectra were recorded using a fluorescent spectrophotometer (F-4600, HITACHI, Japan) with a photomultiplier tube operating at 400 V and a 150 W Xe lamp at room temperature, and the temperature-dependence luminescence properties were measured on the same spectrophotometer combined with a self-made heating attachment and a computer-controlled electric furnace. The room temperature decay curves were recorded on a JOBIN YVON FL3-21 spectro-fluorometer.

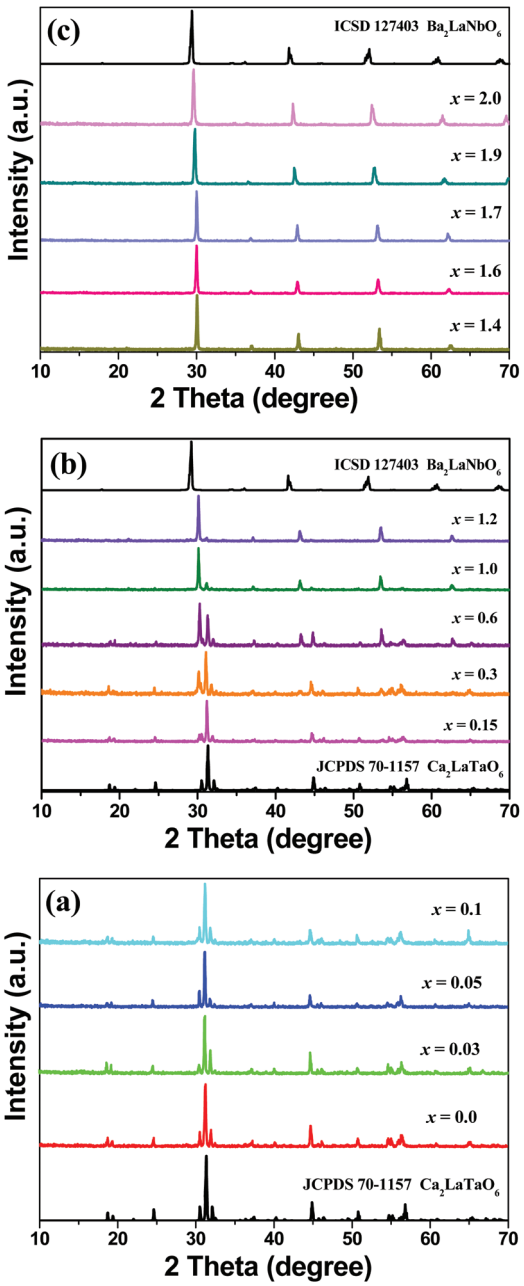

Fig. 1 XRD patterns of the as-prepared $Ca_{(2-x)}Ba_xLaNbO_6$:Eu^{3+} samples and the standard data of $CaLaNbO_6$ (JCPDS 70-1157) and Ba_2LaNbO_6 (ICSD 127403) used as references. (a) x = 0 to 0.1 [phase 1: monoclinic ($P2_1/n$)]. (b) x = 0.15 to 1.2 [the mixed phase]. (c) x = 1.4 to 2 [phase 2: monoclinic ($C2/m$)].

3. Results and discussion

3.1 Phase formation and crystal structure

The phase structures of the as-prepared $Ca_{(2-x)}Ba_xLaNbO_6$:Eu^{3+} phosphors were investigated using powder X-ray diffraction (PXRD) and Rietveld refinements. The PXRD data in Fig. 1 show that the samples could be divided into three sections: part (a) x = 0 to 0.1 [phase 1: monoclinic Ca_2LaNbO_6 ($P2_1/n$)], part (b) x = 0.15 to 1.2 [the mixed phases of Ca_2LaNbO_6 ($P2_1/n$) and Ba_2LaNbO_6 ($C2/m$)], and part (c) x = 1.4 to 2 [phase 2: monoclinic ($C2/m$)] based on the comparison of the standard data of the two end members and the differences in positions and relative intensities of the as-measured diffraction peaks. One can see that all the diffraction peaks of the samples match well with those of the monoclinic phase Ca_2LaNbO_6

(JCPDS 70-1157) and Ba_2LaNbO_6 (ICSD 127403) in Fig. 1a and 1c, and no traces of impurity phases are observed, indicating the successful isomorphic replacement of Ba atoms by Ca atoms in the present structure in the range of $0 \leq x \leq 0.1$ and $1.4 \leq x \leq 2.0$. However, in Fig. 1b with the composition range of $0.15 \leq x \leq 1.2$, the diffraction peaks of the samples represent not only the Ca_2LaNbO_6 phase, but also the Ba_2LaNbO_6 phase, and gradually change from Ca_2LaNbO_6 to Ba_2LaNbO_6. All the diffraction peaks in Fig. 1b can be defined as each of them. Therefore, this section between 0.15 and 1.2 was regarded as the mixed phases of Ca_2LaNbO_6 to Ba_2LaNbO_6.

In order to further recognize the structural phase transitions of the as-prepared phosphors, Rietveld refinements of powder XRD profiles of representative $Ca_{(2-x)}Ba_xLaNbO_6$ (x = 0, 0.3, 1.2, 1.6, 2) were performed by using TOPAS 4.2. The original structure model of previously reported crystallographic data of Ca_2NdNbO_6 (ICSD 86295) and Ba_2LaNbO_6 (ICSD 172403) as the corresponding starting model was employed to refine the above samples and the refinement results are presented in detail in Fig. 2 and Table 1. Powder patterns of compounds with x = 0 and 0.3 were indexed by the monoclinic cell ($P2_1/n$) with parameters close to Ca_2NdNbO_6, and x = 1.2, 1.6 and 2 were indexed by the monoclinic cell ($C2/m$) close to Ba_2LaNbO_6. Small impurities (10%) of the cubic phase $Pm\bar{3}m$ monoclinic phase and (13%) the monoclinic phase Ca_2LaNbO_6 were detected in compounds with x = 0.3 and x = 1.2, respectively. It indicates that with the increase of the Ba content, the crystal structure of the phosphor gradually turns from one monoclinic cell ($P2_1/n$) to another monoclinic cell ($C2/m$).

As shown in Fig. 2f, the crystal structure of Ca_2LaNbO_6 has two different Ca sites, one of them occupied by La and Ca with occupancies 0.5/0.5, respectively, and another site is occupied by Ca only. Compound with x = 0.3 is isostructural to Ca_2LaNbO_6 and it was suggested that Ba ions occupy the Ca/La site instead of the Ca site. This is because Ba ions are bigger than Ca, the coordination number (CN) = 8 of the 4e site occupied only by Ca has more possibility to include bigger ions compared to the 2b site with CN = 6. The concentration of Ca/Ba was fixed according to chemical formula. Refinement of this model was stable and gives low R-factors (Table 1). As shown in Fig. 2g, the independent part of the unit cell Ba_2LaNbO_6 contains one NbO_6 octahedron, one LaO_6 octahedron and one Ba site. It was suggested that Ca ions in compounds with x = 1.2 and 1.6 occupy Ba sites instead of La sites because Ca ions will decrease the amount of La ions and lead to negative total sum of charge. Refinement of this model was also stable and gives low R-factors (Table 1).

Accordingly, the lattice parameters a, b, c and the unit cell volume V depending on different Ba contents in the three phase sections are plotted in Fig. 3. It was concluded from the calculated cell parameters that the phase transition between $P2_1/n$ and $C2/m$ phases exists in the range of x = 0.3–1.2. The Ba content dependence of cell parameters proves that a, b, c show a jump and β also shows a jump and even different behaviors in this range for the designed $Ca_{(2-x)}Ba_xLaNbO_6$

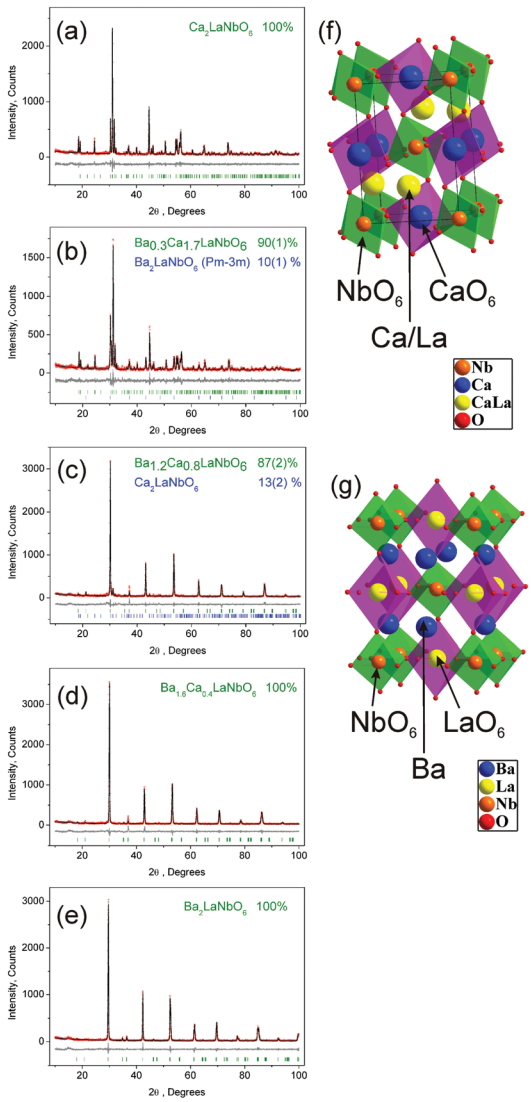

Fig. 2 Difference Rietveld plot of $Ca_{(2-x)}Ba_xLaNbO_6:Eu^{3+}$ samples and the crystal structure of Ca_2LaNbO_6 and Ba_2LaNbO_6. (a) x = 0. (b) x = 0.3. (c) x = 1.2. (d) x = 1.6. (e) x = 2.0. (f) Crystal structure of Ca_2LaNbO_6. (g) Crystal structure of Ba_2LaNbO_6.

(Fig. 3a–3d). The cell parameters of the $C2/m$ phase were transformed according to the formula: $a' = (a^2 + c^2 - 2ac\cos\beta)^{1/2}$; $b' = b$; $c' = a$, $\beta' = \arccos((c - a\cos\beta)/a')$ to allow easier comparison with the cell parameters a, b, c, β of the $P2_1/n$ phase. However, the cell volume shows a smooth linear increase with x in agreement with the ion radii of Ba and Ca, as can be found from Fig. 3e.

3.2 Luminescence properties

As we know, Eu^{3+} ions act as the structural probes to study structural phase transitions, which contain the magnetic dipole transition $^5D_0$–$^7F_1$ at about 596 nm and the electric dipole transition $^5D_0$–$^7F_2$ at about 618 nm. The emission intensity is normally hypersensitive to the crystal environment of

Table 1 Main parameters of processing and refinement of the $Ca_{(2-x)}Ba_xLaNbO_6$ samples

x Value	0	0.3		1.2		1.6	2
Phases	Ca_2LaNbO_6	$Ba_{0.3}Ca_{1.7}LaNbO_6$	Ba_2LaNbO_6	$Ba_{1.2}Ca_{0.8}LaNbO_6$	Ca_2LaNbO_6	$Ba_{1.6}Ca_{0.4}LaNbO_6$	Ba_2LaNbO_6
Weight, %	100	90(1)	10(1)	87(2)	13(2)	100	100
Sp.Gr.	$P2_1/n$	$P2_1/n$	$Pm\bar{3}m$	$C2/m$	$P2_1/n$	$C2/m$	$C2/m$
a, Å	5.6139(3)	5.6225(5)	4.1884(4)	10.2630(16)	5.628(1)	10.3628(18)	10.4771(12)
b, Å	5.8656(3)	5.8692(5)	—	5.9329(6)	5.884(2)	5.9652(11)	6.0588(6)
c, Å	8.1157(4)	8.1296(7)	—	5.9398(8)	8.123(2)	5.9606(12)	6.0309(7)
β, °	90.161(3)	90.151(8)	—	125.275(11)	90.15(3)	125.34(9)	125.386(6)
V, Å^3	267.24(2)	268.27(4)	73.47(2)	295.26(8)	269.0(1)	300.6(1)	312.11(6)
Z	2	2	1	2	2	2	2
2*θ*-Interval, °	10–100	10–100		10–100		10–100	10–100
No. reflections	275	275	18	172	276	172	183
No. refined parameters	38	50		67		41	41
R_{wp}, %	12.90	14.46		16.44		16.51	15.00
R_p, %	9.92	11.29		12.02		11.79	10.81
R_{exp}, %	11.23	11.79		12.32		12.60	13.27
χ^2	1.15	1.23		1.34		1.31	1.13
R_B, %	2.24	4.34	2.90	2.90	8.75	2.98	2.16

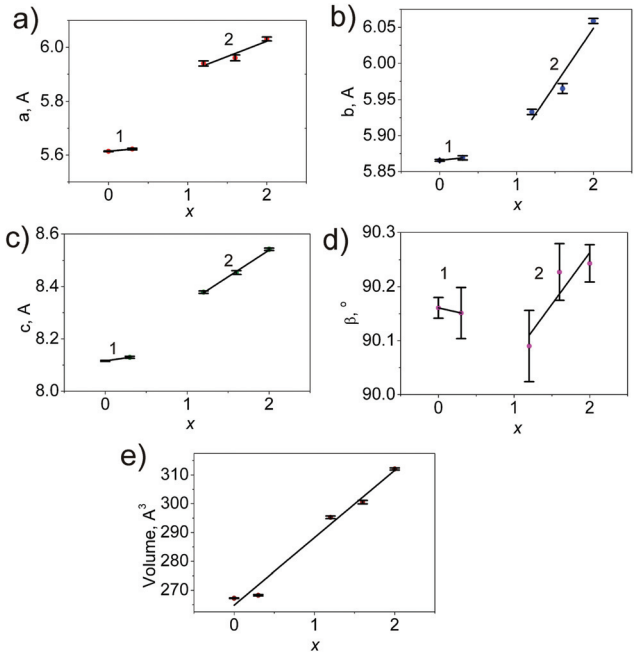

Fig. 3 The Ba content dependence of cell parameters: (a) *a* of $P2_1/n$ phase (1), *c* of *C*2/*m* phase (2); (b) *b* of $P2_1/n$ phase (1), *b* of *C*2/*m* phase (2); (c) *c* of $P2_1/n$ phase (1), $a' = (a^2 + c^2 - 2ac\cos\beta)^{1/2}$ of *C*2/*m* phase (2); (d) *β* of $P2_1/n$ phase (1), $\beta' = \arccos((c - a\cos\beta)/a')$ of *C*2/*m* phase (2); (e) cell volume of all phases.

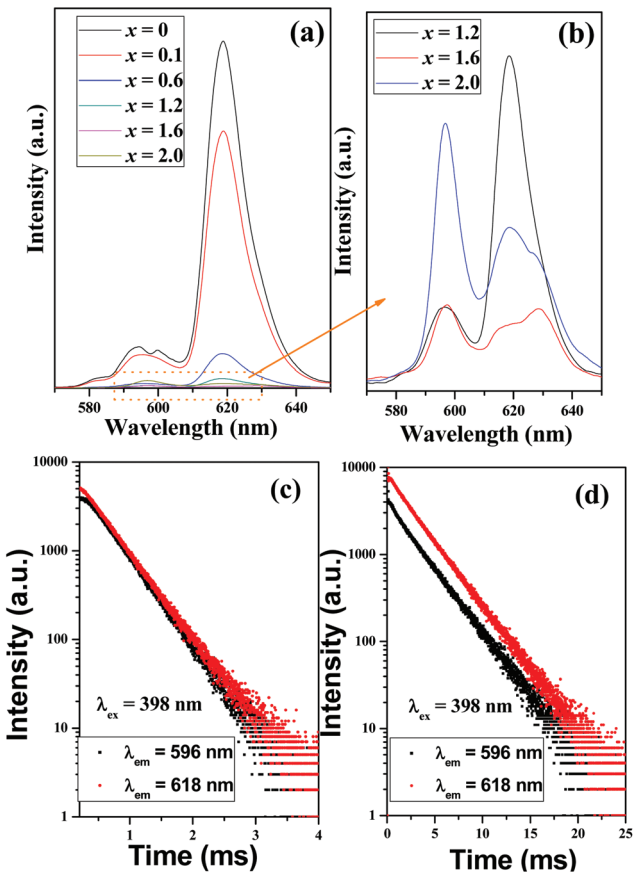

Fig. 4 PL spectra of $Ca_{(2-x)}Ba_xLaNbO_6:Eu^{3+}$ samples upon excitation at 398 nm, (a) $x = 0$ to 2. (b) The enlarged spectral profiles for $x = 1.2$, 1.6 and 2.0. PL decay curves of the two end members $Ca_2LaNbO_6:Eu^{3+}$ (c) and $Ca_2LaNbO_6:Eu^{3+}$ (d) by monitoring different transitions at 596 and 618 nm.

Eu^{3+} ions. That's to say, the evolution of the emission ratio $(^5D_0-^7F_2)/(^5D_0-^7F_1)$ depends on the variation of Eu^{3+} ion site symmetry. The emission transition is mainly $^5D_0-^7F_2$ (618 nm) from the Eu^{3+} sites without inversion symmetry; otherwise, the transition is mainly $^5D_0-^7F_2$ (596 nm) with inversion symmetry. Therefore, in order to link the relationship between luminescence properties and crystal structure, the photoluminescence (PL) emission spectra of this series of $Ca_{(2-x)}Ba_xLaNbO_6:Eu^{3+}$ samples are given in Fig. 4a; it is found that the PL intensities decrease sharply with the decrease of Ca/Ba ratios, which means that strong red emission from $^5D_0-^7F_2$ peaking at 618 nm can be found in $Ca_2LaNbO_6:Eu^{3+}$. Fig. 4a shows the enlarged spectral profiles of the selected samples of

$Ca_{(2-x)}Ba_xLaNbO_6:Eu^{3+}$ for x = 1.2, 1.6 and 2.0, and we can find that the emission ratio $(^5D_0–^7F_2)/(^5D_0–^7F_1)$ changes when the compositions are located in the above-mentioned part (c) of Ba_2LaNbO_6 phases. As we know, Eu^{3+} will enter the La sites in this series of $Ca_{(2-x)}Ba_xLaNbO_6$ compounds from the consideration of charge balance and the similar ionic radius; however, the La sites are disordered in the Ca_2LaNbO_6 phase, so that the doped Eu^{3+} ions at highly distorted eight-coordinated sites can rapidly promote the probability of an electric dipole transition to emit intense red light at 618 nm. As a comparison, the crystal structures of $Ca_{(2-x)}Ba_xLaNbO_6$ (x = 1.4–2.0) belong to a relatively ordered environment than that of Ca_2LaNbO_6; the transition probability of Eu^{3+} in such a system will decrease and the orange emission originating from 598 nm will predominate among the observed Eu^{3+} emission lines. Furthermore, the PL decay curves of the two end members $Ca_2LaNbO_6:Eu^{3+}$ and $Ba_2LaNbO_6:Eu^{3+}$ by monitoring different transitions at 596 and 618 nm have been demonstrated in Fig. 4c and 4c, respectively, in order to probe more luminescence dynamic information. All the decay curves can be well fitted using a first-order exponential decay formula:

$$I(t) = I_0 + A\exp(-t/\tau) \quad (1)$$

where I and I_0 are the luminescence intensities at time t and 0, A is a constant, t is the time, and τ represents the decay time for an exponential component. The decay curves indicate that all Eu^{3+} ions occupy the same crystal environment, which is consistent with the description of the crystal structure above. On the basis of the results of single exponential decay fitting, the lifetime values of the $^5D_0–^7F_1$ transition at 596 nm and the $^5D_0–^7F_2$ transition at 618 nm of $Ca_2LaNbO_6:Eu^{3+}$ phosphors were calculated to be 4.51 and 4.47 ms, respectively. As for $Ba_2LaNbO_6:Eu^{3+}$ phosphors, the corresponding values are 2.91 and 2.85 ms. The low lifetime values of $Ba_2LaNbO_6:Eu^{3+}$ also verify the fast energy transfer between the emission centres and the induced emission quenching, which is in agreement with the low emission intensities compared to $Ca_2LaNbO_6:Eu^{3+}$.

Fig. 5 show a careful analysis of the Ca/Ba ratio dependence of the normalized emission intensities of this series of $Ca_{(2-x)}Ba_xLaNbO_6:Eu^{3+}$ samples (x = 0–2) under 398 nm excitation. The emission intensity is normally relative to the crystal environment of Eu^{3+} ions.[14,15] As shown in Fig. 5a, with increasing Ba content in the range of $0 \le x \le 0.1$, the as-prepared phosphor exhibits the same features of four main bands with maxima at about 596, 618, 660, and 706 nm, due to the $^5D_0 \rightarrow {}^7F_J$ (J = 1, 2, 3, 4) transitions. In addition, it can be found that the intensity of the $^5D_0 \rightarrow {}^7F_1$ magnetic-dipole transition (596 nm) is weaker than that of the $^5D_0 \rightarrow {}^7F_2$ electric-dipole transition (618 nm). In Fig. 5b and c, the $^5D_0 \rightarrow {}^7F_1$ magnetic-dipole transition (596 nm) becomes more and more intense by increasing Ba^{3+} in $Ca_{(2-x)}Ba_xLaNbO_6:Eu^{3+}$. As mentioned above, the ratio between the magnetic-dipole transition (596 nm) and the electric-dipole transition (618 nm) can help to deeply understand the difference of symmetry of the Eu^{3+} sites, and the evolution of this value depends on the variation of Eu^{3+} ion site symmetry. As shown in Fig. 5d, the $Ratio_{596/618}$ keeps instantly. In this case, the Eu^{3+} ions from EuO_8 dodecahedra of the Ca_2LaNbO_6 phase are located at a low symmetry, the electric-dipole transition is no longer strictly forbidden and hypersensitive emission of $^5D_0 \rightarrow {}^7F_2$ should be the dominant one, according to the Judd–Ofelt theory.[16,17] When the Ba contents are located in the range of $0.15 \le x \le 1.2$, the intensity $Ratio_{596/618}$ increases slightly in the mixed phases. However, the $Ratio_{596/618}$ increases apparently with the increase of the Ba content from 1.4 to 2.0. Under the circumstances, Eu^{3+} ions located at the six-coordinated sites (EuO_6) of the Ba_2LaNbO_6 phase are an inversion symmetry site. The electric-dipole transition is strictly forbidden. So the emission of 618 nm ($^5D_0 \rightarrow {}^7F_2$ electric-dipole transition) is very weak.

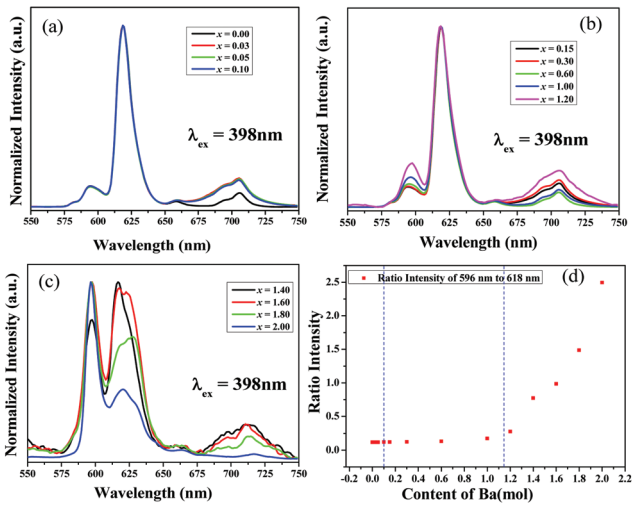

Fig. 5 Normalized PL spectra of $Ca_{(2-x)}Ba_xLaNbO_6:Eu^{3+}$ samples. (a) x = 0 to 0.1. (b) x = 0.15 to 1.2. (c) x = 1.4 to 2. (d) PL intensity ratio of 596 to 618 nm.

The UV-vis diffuse reflectance spectra of the selected $Ca_{(2-x)}Ba_xLaNbO_6:Eu^{3+}$ samples for different Ba contents are illustrated in Fig. 6. It is clearly found that the absorption of $Ca_{(2-x)}Ba_xLaNbO_6:Eu^{3+}$ samples is located at the two regions: one part between 200 and 380 nm is ascribed to the absorption band from the $O^{2-} \rightarrow Eu^{3+}$ charge transfer transition, and the other absorption lines located at 393, 465 and 533 nm originate from the f–f transitions of Eu^{3+}. The above results verified that the as-prepared phosphors can absorb both UV light and the characteristic excitation light of Eu^{3+} in the near-UV region (393 nm) and the blue light region (465 nm), which is beneficial to the application as red phosphors for near-UV or blue light pumped white LEDs.

As a contrast, the PLE spectra of this series of $Ca_{(2-x)}Ba_xLaNbO_6:Eu^{3+}$ samples (x = 0–2) are also shown in Fig. 6. The excitation spectra can be divided into two regions: the sharp peaks in the range of 350–500 nm are associated with the $^5D_0 \rightarrow {}^7F_J$ (J = 1, 2, 3, 4) transitions of Eu^{3+}, respectively. A broad band absorption peak in the range of 200–350 nm

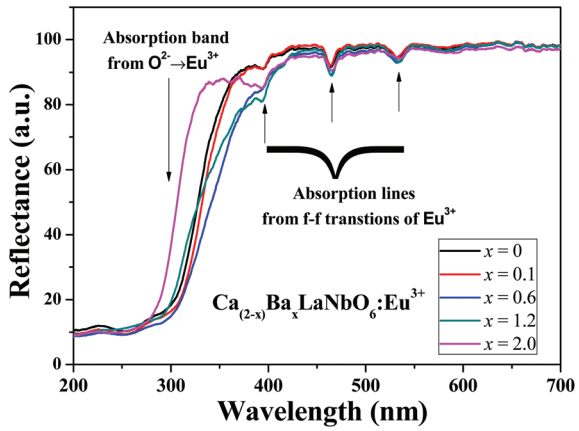

Fig. 6 UV-vis diffuse reflectance spectra of $Ca_{(2-x)}Ba_xLaNbO_6:Eu^{3+}$ samples for different Ba contents, x = 0, 0.1, 0.6, 1.2 and 2.0.

with a peak maximum at about 305 nm is mainly related to the charge transfer (CT) transitions of ligand O^{2-} atoms to Eu^{3+} since the position of the $O^{2-} \rightarrow Eu^{3+}$ charge transfer band (CTB) is usually located in the range of 170–260 nm in most hosts.[18–20] It is clear that all of the PLE spectra have a similar shape when monitored at 596 nm (Fig. 7a, c and e) and 618 nm (Fig. 7b, d and f) (Eu^{3+} emission) except for the difference of the CT position. In addition, with the replacement of Ba with Ca ions, the relative intensity of the charge transfer transitions was enhanced gradually. From the excitation spectra, it is clearly found that the present niobate phosphors can be excited by both the near ultraviolet (396 nm) and the blue light (465 nm), matching well with the emission wavelength of the commercial LED chips currently in LED devices.[21–23]

3.3 The thermally stable luminescence

As is well known, the thermal stability of phosphors is one of the important issues in their practical application.[24,25] In order to further characterize the properties of the phosphors depending on the environment temperature, Fig. 8 presents the emission spectra of selected $Ca_{(2-x)}Ba_xLaNbO_6:Eu^{3+}$ (x = 0, 0.6, 1, 1.2, 1.4, 2) phosphors at different temperatures. One can see that while the content of Ba was in the range of $0 \leq x \leq 1.2$, both the emission intensities of the magnetic-dipole transition (596 nm) emission spectrum and the electric-dipole transition (618 nm) decrease progressively with the increase of temperature as shown in Fig. 8a–d. However, the emission intensities of the spectrum turn out to be in the opposite situation when the content of Ba was 1.4 and 2 in Fig. 8e and f. As we discussed previously, the phase structures

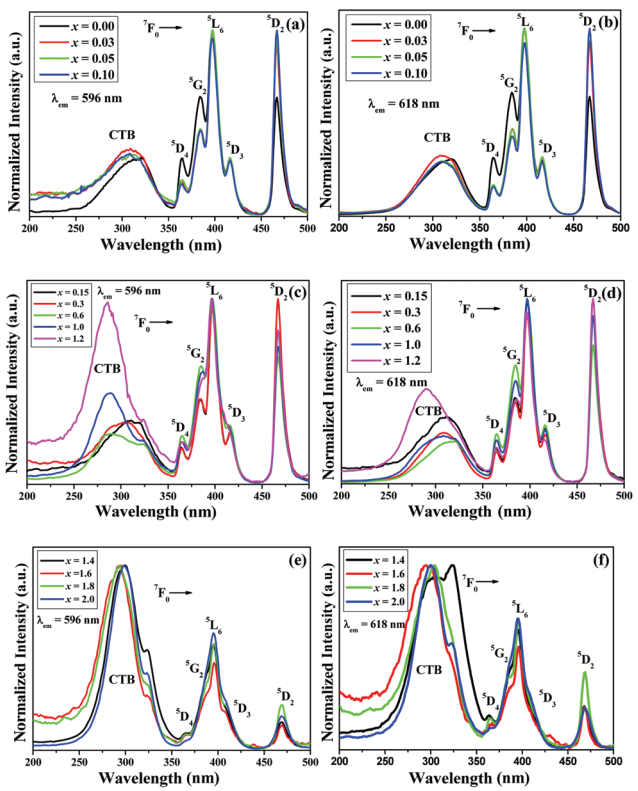

Fig. 7 Normalized PLE spectra of $Ca_{(2-x)}Ba_xLaNbO_6:Eu^{3+}$ samples under 596 and 618 nm excitation, respectively. (a) and (b) x = 0 to 0.1. (c) and (d) x = 0.15 to 1.2. (e) and (f) x = 1.4 to 2.

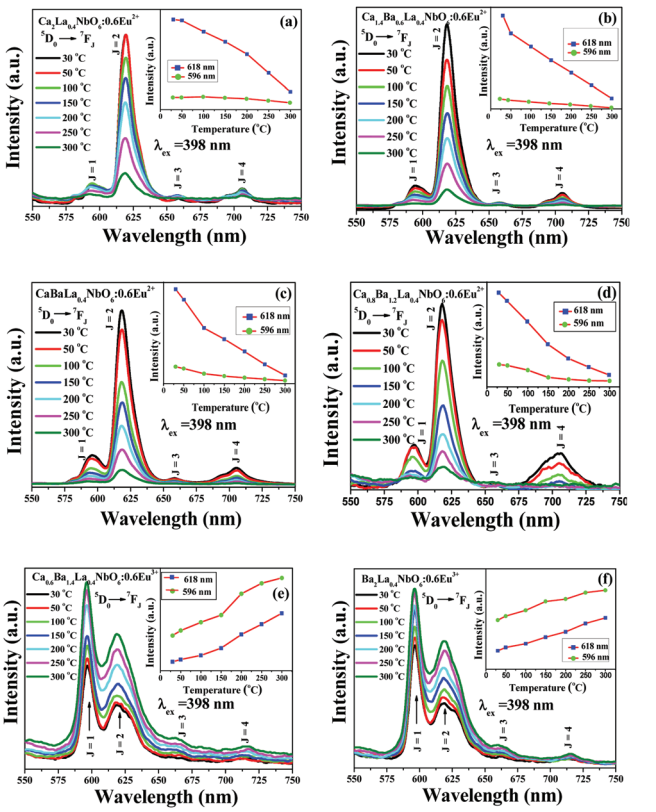

Fig. 8 The PL spectra (λ_{ex} = 398 nm) of the $Ca_{(2-x)}Ba_xLaNbO_6:Eu^{3+}$ phosphor under different temperatures in the range of 30–300 °C. (a) x = 0, (b) x = 0.6, (c) x = 1, (d) x = 1.2, (e) x = 1.4 and (f) x = 2.

in such a composition range (x = 1.4–2.0) are iso-structural with the monoclinic ($C2/m$) Ba_2LaNbO_6 structure, which contains one NbO_6 octahedron, one LaO_6 octahedron and one Ba site. Eu^{3+} emission intensities in such a structure increased with the increase of temperature; therefore, it means that the transition probability of the activators increase in such a host with the help of the decreased site symmetry. Ca_2LaNbO_6 ($P2_1/n$) is more distorted than Ba_2LaNbO_6 because it has lower symmetry, and Ba_2LaNbO_6 ($C2/m$) is the parent phase of the distorted ($P2_1/c$) phase. So the observed different temperature dependent luminescence behaviours are also in agreement with the tunable structural character depending on the chemical compositions and temperature of the double perovskite compounds.[26,27]

4. Conclusion

In summary, a series of $Ca_{(2-x)}Ba_xLaNbO_6$:Eu^{3+} ($0 \leq x \leq 2$) phosphors have been synthesized by the conventional high temperature solid-state reaction route. The structural phase transitions depending on Ca/Ba ratios from Ca_2LaNbO_6 to Ba_2LaNbO_6 were studied *via* X-ray diffraction analysis, and further probed by the characteristic red emission of Eu^{3+}. The XRD patterns revealed that phases are divided into three sections including the disordered Ca_2LaNbO_6, the ordered Ba_2LaNbO_6 and the mixed phases between them. Due to the different Ca/Ba ratios, the lattice constants exhibited different tendency for linear variation. Moreover, when Eu^{3+} ions occupy the site without inversion symmetry, it shows the strongest red emission line at 618 nm corresponding to the $^5D_0 \rightarrow {}^7F_2$ transition, and Ca_2LaNbO_6:Eu^{3+} phosphors can act as the potential red phosphors for white LEDs. While Eu^{3+} ions in Ba_2LaNbO_6 occupy the inversion symmetry site, the emission intensities were weak, and the magnetic-dipole transition (596 nm) predominated. The thermal stability luminescence also verified that the different phase structures will also affect the variation of the emission intensities depending on the temperature. This study can serve as a guide to discuss the structural phase transformation *via* the combined techniques of X-ray diffraction and Eu^{3+} probes, and will also help to explore the new luminescence materials with controllable optical properties induced by the variation of the local coordination environment.

Acknowledgements

The present work was supported by the National Natural Science Foundation of China (Grant No. 51272027, 51472028 and 51272242), Natural Science Foundations of Beijing (2132050), the Program for New Century Excellent Talents in the University of the Ministry of Education of China (NCET-12-0950), Beijing Nova Program (Z131103000413047), Beijing Youth Excellent Talent Program (YETP0635), and the Funds of the State Key Laboratory of New Ceramics and Fine Processing, Tsinghua University (KF201306).

Notes and references

1 Y. Shimizu, S. Sakagami, K. Goto, Y. Nakachi and K. Ueda, *Mater. Sci. Eng., B*, 2009, **161**, 100–103.
2 B. Ranjbar, A. Pavan, B. J. Kennedy and Z. M. Zhang, *Dalton Trans.*, 2015, **44**, 10689–10699.
3 A. Faik, E. Iturbe-Zabalo, I. Urcelay and J. M. Igartua, *J. Solid State Chem.*, 2009, **182**, 2656–2663.
4 P. A. Tanner and Z. F. Pan, *Inorg. Chem.*, 2009, **48**, 11142–11146.
5 X. Yin, Y. M. Wang, F. Q. Huang, Y. J. Xia, D. Y. Wan and J. Y. Yao, *J. Solid State Chem.*, 2011, **184**, 3324–3328.
6 V. S. Fillipev and E. G. Fesenko, *Sov. Phys. Crystallogr.*, 1966, **10**, 243–247.
7 W. Meng and A. V. Virkar, *J. Solid State Chem.*, 1999, **148**, 492–498.
8 A. M. Srivastava and M. G. Brik, *J. Lumin.*, 2012, **132**, 579–584.
9 A. Dutta, S. Saha, P. Kumari, T. P. Sinha and S. Shannigrahi, *J. Solid State Chem.*, 2015, **229**, 296–302.
10 W. T. Fu and D. J. W. IJdo, *J. Solid State Chem.*, 2006, **179**, 1022–1028.
11 W. Lv, W. Z. Lv, Q. Zhao, M. M. Jiao, B. Q. Shao and H. P. You, *Inorg. Chem.*, 2014, **53**, 11985–11990.
12 Q. Zhou, Y. Y. Zhou, Y. Liu, L. J. Luo, Z. L. Wang, J. H. Peng, J. Yan and M. M. Wu, *J. Mater. Chem. C*, 2015, **3**, 3055–3059.
13 J. S. Zhong, D. Q. Chen, W. G. Zhao, Y. Zhou, H. Yu, L. F. Chen and Z. G. Ji, *J. Mater. Chem. C*, 2015, **3**, 4500–4510.
14 D. Vandervort and G. Blasse, *Chem. Mater.*, 1991, **3**, 1041–1045.
15 T. Montini, A. Speghini, L. De Rogatis, B. Lorenzut, M. Bettinelli, M. Graziani and P. Fornasiero, *J. Am. Chem. Soc.*, 2009, **131**, 13155–13160.
16 S. Shionoya and W. M. Yen, *Phosphor Handbook*, CRC Press, Boca Raton, FL, 1999, 88–179.
17 T. R. Zhang, C. Spitz, M. Antonietti and C. F. J. Faul, *Chem. – Eur. J.*, 2005, **11**, 1001–1009.
18 L. Li, X. G. Liu, H. M. Noh, S. H. Park, J. H. Jeong and K. H. Kim, *J. Alloys Compd.*, 2015, **620**, 324–328.
19 I. P. Roof, M. D. Smith, S. Park and H. C. zur Loye, *J. Am. Chem. Soc.*, 2009, **131**, 4202–4203.
20 M. Mohapatra, B. Rajeswari, N. S. Hon, R. M. Kadam and V. Natarajan, *J. Lumin.*, 2015, **166**, 1–7.
21 P. L. Shi, Z. G. Xia, M. S. Molokeev and V. V. Athchi, *Dalton Trans.*, 2014, **43**, 9669–9676.
22 F. C. Lu, L. J. Bai, Z. P. Yang and Q. L. Liu, *J. Rare Earths*, 2012, **30**, 851–855.
23 J. Y. Sun, G. C. Sun and Y. N. Sun, *Ceram. Int.*, 2014, **40**, 1723–1727.

24 J. Q. Liu, X. J. Wang, T. T. Xuan, C. B. Wang, H. L. Li and Z. Sun, *J. Lumin.*, 2015, **158**, 322–327.
25 F. F. Zhang, K. X. Song, J. Jiang, S. Wu, P. Zheng, Q. M. Huang, J. M. Xu and H. B. Qin, *J. Alloys Compd.*, 2014, **615**, 588–593.
26 P. J. Saines, B. J. Kennedy and M. M. Elcombe, *J. Solid State Chem.*, 2007, **180**, 401–409.
27 B. Orayech, I. Urcelay-Olabarria, G. A. Lopez, O. Fabelo, A. Faik and J. M. Igartua, *Dalton Trans.*, 2015, **44**, 13867–13880.